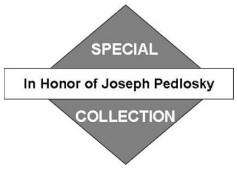

Buoyancy-Forced Downwelling in Boundary Currents

MICHAEL A. SPALL

Woods Hole Oceanographic Institution, Woods Hole, Massachusetts

(Manuscript received 31 January 2008, in final form 27 May 2008)

ABSTRACT

The issue of downwelling resulting from surface buoyancy loss in boundary currents is addressed using a high-resolution, nonhydrostatic numerical model. It is shown that the net downwelling is determined by the change in the mixed layer density along the boundary. For configurations in which the density on the boundary increases in the direction of Kelvin wave propagation, there is a net downwelling within the domain. For cases in which the density decreases in the direction of Kelvin wave propagation, cooling results in a net upwelling within the domain. Symmetric instability within the mixed layer drives an overturning cell in the interior, but it does not contribute to the net vertical motion. The net downwelling is determined by the geostrophic flow toward the boundary and is carried downward in a very narrow boundary layer of width $E^{1/3}$, where E is the Ekman number. For the calculations here, this boundary layer is O(100 m) wide. A simple model of the mixed layer temperature that balances horizontal advection with surface cooling is used to predict the net downwelling and its dependence on external parameters. This model shows that the net sinking rate within the domain depends not only on the amount of heat loss at the surface but also on the Coriolis parameter, the mixed layer depth (or underlying stratification), and the horizontal velocity. These results indicate that if one is to correctly represent the buoyancy-forced downwelling in general circulation models, then it is crucial to accurately represent the velocity and mixed layer depth very close to the boundary. These results also imply that processes that lead to weak mixing within a few kilometers of the boundary, such as ice formation or freshwater runoff, can severely limit the downwelling forced by surface cooling, even if there is strong heat loss and convection farther offshore.

1. Introduction

The heat and freshwater carried by the oceanic thermohaline circulation comprises a fundamental component of the earth's climate system. The prototypical example is the North Atlantic Ocean. Warm, salty water is carried northward in the upper ocean where, at high latitudes, the water becomes both colder and fresher, resulting in dense water masses that return to low latitudes in the middepth and deep ocean. Much attention has been paid to where and how deep waters return to the upper ocean (e.g., Polzin et al. 1997). However, the processes by which the upper ocean waters sink has been much less explored. Here, a specific point needs to be clarified. Sinking refers to downwelling in Eulerian space. This is different from the process by which waters become more dense and downwell in density space, which can take place without any net vertical motion (Send and Marshall 1995). Interest in the vertical velocity arises not only because it is a basic component of the three-dimensional circulation but also from its fundamental importance for the vorticity balance of the fluid. While the thermohaline circulation is often discussed in the context of the Atlantic Ocean, there are analogous circulations in numerous marginal seas, some in the Atlantic Ocean, in which water mass transformation takes place, such as the Greenland–Iceland–Norwegian (GIN) Seas, Labrador Sea, Mediterranean Sea, Adriatic Sea, and Persian Gulf.

While the thermohaline circulation is often depicted as a two-dimensional flow in the latitude-depth plane—and is sometimes even referred to as the meridional overturning circulation—such a simplification masks what in reality is a much more complicated three-dimensional system of currents. Analysis of hydrographic data or high-resolution numerical models indicates that the northward-flowing warm waters in the North Atlantic and GIN Seas are found in the eastern basin and the southward-flowing colder waters are found in the western basin (Mauritzen 1996a). On

Corresponding author address: Michael Spall, WHOI, MS#21, 360 Woods Hole Road, Woods Hole, MA 02543.
E-mail: mspall@whoi.edu

DOI: 10.1175/2008JPO3993.1

average, the southward-flowing waters in the west are deeper than the northward-flowing waters in the east, reflecting a net downwelling somewhere at high latitudes as the water flows cyclonically around the basin. However, there is generally southward flow throughout the water column along the western boundary with cold waters at the surface, indicating that there is also a strong horizontal component to the circulation and heat transport. Early descriptions of this process assumed that the regions where the waters sank to deeper depths were the same as the regions where the waters became more dense. Although large buoyancy loss clearly drives water mass transformation in the interior of many basins, observations, modeling, and theoretical studies all suggest that the net downwelling in regions of buoyancy loss in the interior of the ocean is negligible (Schott et al. 1993; Send and Marshall 1995; Marotzke and Scott 1999; Marshall and Schott 1999; Spall 2003, 2004). There is intense downwelling of dense water concentrated within narrow plumes with lateral scale O(1 km), but outside of these plumes there is weaker, broader upwelling of less-dense water (Schott et al. 1993; Steffen and D'Asaro 2002). Spatial averages of vertical velocity are difficult to obtain directly from observations, although Schott et al. find near zero mean vertical velocity from temporal averages at a point. However, high-resolution, nonhydrostatic numerical model calculations indicate that there is no net vertical volume flux in interior regions of deep convection, although there is a vertical density flux (Send and Marshall 1995). Consideration of the vorticity balance quickly reveals that to get any significant downwelling in the ocean interior, one must generate either large relative vorticity (Send and Marshall 1995) or a large recirculating gyre that advects planetary vorticity (Spall and Pickart 2001), neither of which is observed in the ocean. So, one must look elsewhere to find where and how the waters of the thermohaline circulation downwell.

There are several ways in which waters can downwell, and regions near boundaries and topography are likely to be favored because dissipation can be large enough to balance the stretching of planetary vorticity. In a stratified ocean with horizontal mixing of momentum and density, downwelling is carried in a hydrostatic boundary layer of width proportional to the internal deformation radius times the square root of a Prandtl number (Barcilon and Pedlosky 1967; Spall 2003; Pedlosky 2003). This mechanism relies on horizontal mixing and stratification, and it is not effective if the diapycnal mixing is weak. It is well known that downstream of sills, dense waters move downslope to balance dissipation in the Ekman layer (Price and Barringer 1994). There is also entrainment and downwelling into the overflow waters in regions of large Froude number as they flow over the sill and descend the slope, thus increasing their transport significantly downstream of sills.

There is clearly a distinct and separate process resulting from surface buoyancy forcing that is responsible for the sinking of the dense waters within the marginal sea that produced the dense overflow waters. There is also downwelling in less constrained regions of buoyancy loss, such as the Labrador Sea (Pickart and Spall 2007). Several recent studies have considered the formation of dense waters on shelves by local surface forcing and its subsequent spreading by baroclinic instability (e.g., Gawarkiewicz and Chapman 1995; Jiang and Garwood 1996), which includes a downwelling component. While there are some regions and times for which this localized, isolated forcing is applicable, over most of the high latitude and marginal seas there exist strong cyclonic boundary currents that have not been considered in these problems (Cuny et al. 2002; Mauritzen 1996a,b). These boundary currents transport large amounts of heat and freshwater into/out of the basins and are primarily responsible for the net exchanges that connect the high latitude and marginal seas with the rest of the world's oceans. The dynamics and thermodynamics of such buoyancy-forced boundary currents, and their role in the thermohaline circulation, are the focus of this study.

2. Example of a buoyancy-forced boundary current

An example of a buoyancy-forced boundary current is presented as a means to introduce the problem and approach, and to highlight several aspects of the circulation that result from the surface forcing. More detailed analysis and parameter sensitivity studies of similar flows are provided in the following sections.

A high-resolution numerical model is used to calculate the secondary circulations and vertical motions forced by cooling of a boundary current. The model is the Massachusetts Institute of Technology general circulation model (MITgcm; Marshall et al. 1997) run with nonhydrostatic Boussinesq physics. The model domain is a channel that is 20 km wide, 48 km long, and 500 m deep. The model horizontal grid spacing is 100 m, and the vertical grid spacing is 10 m. Subgrid-scale mixing of momentum and temperature is parameterized by a horizontal Laplacian mixing with coefficients of $1\ \mathrm{m^2\ s^{-1}}$ and vertical mixing coefficients of $10^{-5}\ \mathrm{m^2\ s^{-1}}$.

The initial stratification is uniform with $N^2 = 4.8 \times 10^{-6}\ \mathrm{s^{-2}}$. The model is forced with a specified inflowing velocity in geostrophic balance with the density field

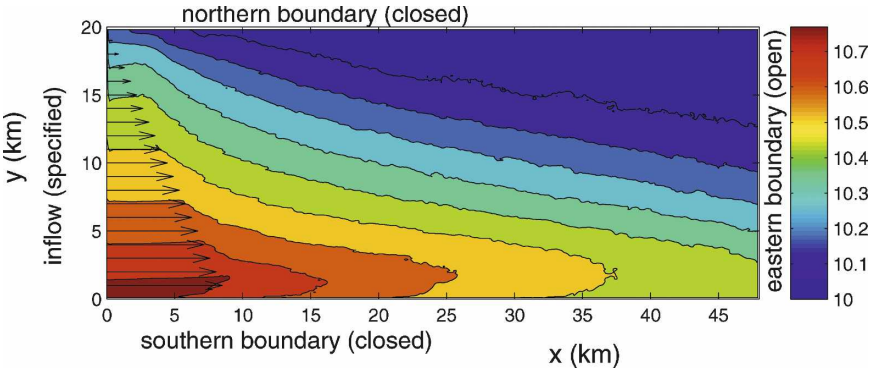

FIG. 1. Temperature at 45-m depth averaged between days 2 and 6 for uniform cooling of 500 W m^{-2} and a velocity field that decays offshore. The velocity at the western (inflowing) boundary is specified and is indicated by vectors. The northern and southern boundaries are closed, but the eastern boundary is open.

and cooled at the surface with a uniform heat flux of 500 W m^{-2} (Fig. 1). The Coriolis parameter is $f_0 = 10^{-4}$ s^{-1} and uniform. The inflowing velocity has a maximum value of 30 cm s^{-1} at the surface on the southern boundary and decreases linearly to zero at 500-m depth and at the northern side of the domain.[1] The model is initialized with this velocity field and a geostrophically balanced density field and sea surface height. The inflow conditions are steady in time, and the outflow boundary conditions for temperature, normal velocity, and tangential velocity are determined by an Orlanski radiation condition (Orlanski 1976; see the MITgcm Web page for details of the numerical implementation: http://mitgcm.org/r2_web_testing/latest/home_page/frontpage.html). The northern and southern lateral boundary conditions are no-normal flow, no-slip, and no-normal heat flux. The initial conditions adjust to the inflow boundary conditions and surface cooling over a time L_x/U, where L_x is the zonal dimension and U is the boundary current velocity, which for the present parameters is O(2–3 days). This model configuration differs from the high-resolution nonhydrostatic models of Haine and Marshall (1998) and Yoshikawa et al. (2001) in several ways; most importantly, their models were in a periodic channel, which did not allow for an along-channel pressure gradient, and their fronts were distant from the lateral boundaries.

The temperature and inflowing velocity at 45-m depth, averaged between days 2 and 6, are shown in Fig. 1. The temperature change across the boundary current at the inflow boundary is approximately 0.45°C. As a result of the surface cooling, the horizontal temperature gradient at the outflowing boundary has been reduced to approximately 0.25°C. The temperature at the offshore side of the current decreases only slightly over the length of the channel, while the temperature of the onshore side of the boundary current decreases by over 0.2°C. The rate of cooling is fastest near the inflow boundary (once cooling has penetrated to this depth, approximately 5 km downstream from the inflow) and decreases downstream. This is because the uniform cooling is distributed over an ever-increasing vertical extent as the mixed layer increases from zero at the inflowing boundary to approximately 200 m at the outflowing boundary. The decrease in lateral temperature gradient from inflow to outflow implies a more barotropic boundary current because, through geostrophy, the vertical shear in the along-channel velocity is related to the lateral density gradient. This implies that there has been a redistribution of mass in the vertical such that the uppermost velocity has decreased and the velocity at some deeper level has increased, requiring a net downwelling within the domain.

Vertical sections of zonal velocity, meridional velocity, temperature, and a meridional/vertical plane streamfunction are plotted in Fig. 2. These quantities were averaged between days 2 and 6, and between $x = 20$ km and $x = 30$ km. An average in the along-channel direction is taken to smooth out small-scale features associated with convection and instabilities in the mixed layer. Because the flow evolves in the downstream direction, the region of averaging is taken to be only a fraction of the full channel length. The mixed layer depth, based on a change in temperature of 0.05°C relative to the sea surface temperature, is indicated by the white line. The most evident change in the zonal velocity is the development of a no-slip boundary

[1] The calculations are all on an f plane but, for convenience, the direction of flow will be considered toward the east and the offshore side of the boundary current will be toward the north.

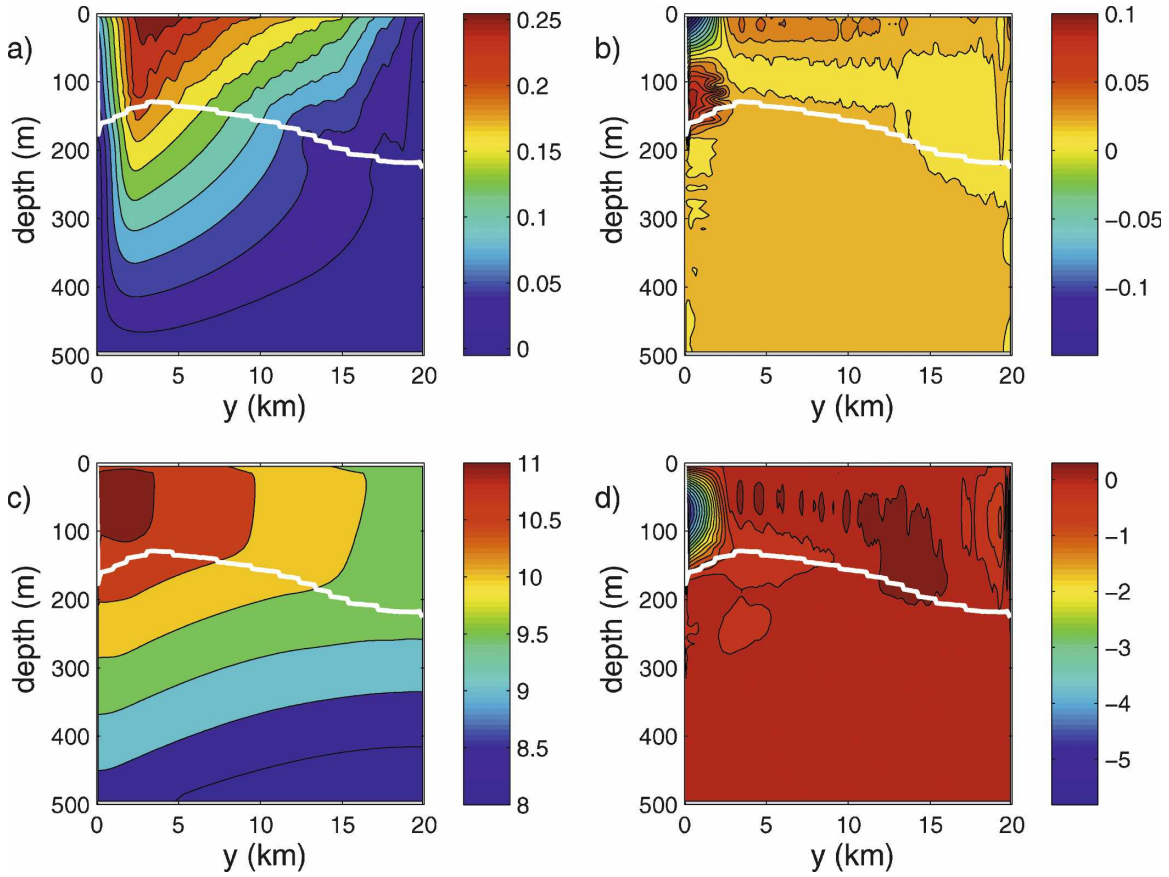

FIG. 2. Vertical section of (a) zonal velocity (m s^{-1}), (b) meridional velocity (m s^{-1}), (c) temperature (°C), and (d) transport streamfunction (10^4 m^3 s^{-1}) averaged between $x = 20$ km and $x = 30$ km between days 2 and 6. The white line indicates the average mixed layer depth.

layer within approximately 2 km of the southern boundary throughout the depth of the domain. The meridional velocity is dominated by two cells, both within the mixed layer (Fig. 2b). The interior (away from the southern boundary) is characterized by northward flow of $O(1\ \text{cm s}^{-1})$ in the upper portion of the mixed layer and southward flow of similar magnitude in the lower mixed layer. The sense of this cross-channel circulation is to restratify the mixed layer. Near the southern boundary, the meridional flow is $O(10\ \text{cm s}^{-1})$ and toward the boundary in the upper mixed layer and away from the boundary in the lower mixed layer. The temperature field shows weak stratification within the mixed layer and a temperature inversion very close to the surface (Fig. 2c).

A meridional/depth transport streamfunction has been calculated by integrating the vertical velocity between $x = 20$ km and $x = 30$ km, and then integrating from the southern boundary to the northern boundary at each depth, with $\psi = 0$ at $y = 0$, so that the streamfunction has units of m^3 s^{-1}. Although the flow in this plane is divergent ($\partial u/\partial x \neq 0$), the streamfunction presented here is a useful way to visualize the ageostrophic motions that characterize the vertical velocity in the interior because $(v_a, w) = (\psi_z, -\psi_y)$, where v_a is the ageostrophic meridional velocity. The vertical motions characterize only the ageostrophic meridional velocity because the geostrophic flow is horizontally nondivergent. The vertical motions are contained primarily in the mixed layer (Fig. 2d). There is a very strong cell adjacent to the southern wall that extends from the surface down to the bottom of the mixed layer, with intense downwelling adjacent to the boundary and weaker upwelling spread over 2–3 km near the wall. The maximum vertical velocities are several centimeters per second directly next to the wall. There is a weaker cell near the northern wall with upwelling next to the boundary and downwelling just offshore. Within the basin interior, the overturning cell is composed largely of weak, closed cells in the direction of restratification, with upwelling of warmer water and downwelling of colder water.

The vertical velocities are locally much larger than the net vertical motion. There are several different processes active, giving rise to different vertical velocities in different parts of the domain. The quantity of interest is the overall net vertical motion, indicated by the average vertical transport as a function of depth calculated between days 2 and 6 and between $x = 20$ km and $x = 30$ km and $y = 0$ km and $y = 20$ km, as shown in Fig. 3. There is downwelling over most of the upper ocean, increasing from zero at the surface to a maximum of almost 6000 $m^3 s^{-1}$ at 100-m depth. Most of the net vertical motion is contained in the mixed layer (the average mixed layer depth over this region is indicated on the figure by the dashed line).

The flow in this calculation is very complicated and reflects influences of not only the large-scale surface forcing and boundary conditions but also instabilities in both the interior and near the boundary. The vertical velocities are influenced by each of these aspects of the flow, making it difficult to sort out their relative contributions. To help unravel the causes of the vertical motions, a series of more idealized calculations is now carried out.

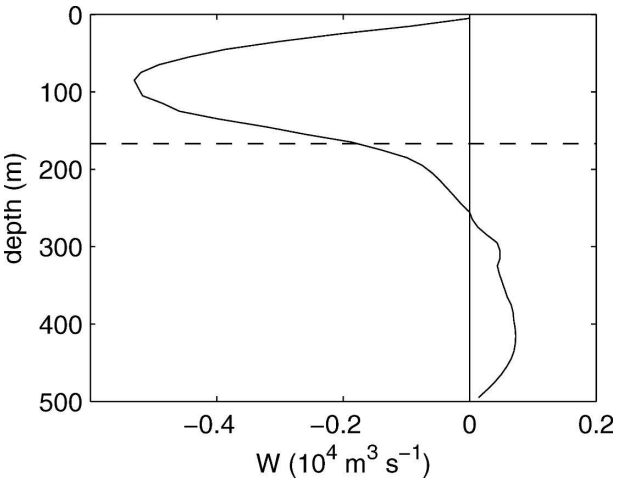

FIG. 3. Vertical mass transport averaged between $x = 20$ km and $x = 30$ km between days 2 and 6. The average mixed layer depth is indicated by the dashed line.

3. Idealized cases

The essential feature of the previous calculation that results in a net downwelling is the decrease in mixed layer density change across the current in the downstream direction. This results from having weaker horizontal advection and a deeper mixed layer on the offshore side of the front than near the southern boundary while having a uniform heat loss at the surface. The deeper mixed layer occurs because the horizontal velocity is weaker on the offshore side of the front, thus resulting in deeper mixing for the same heat loss. However, a similar density field arises if the horizontal velocity is uniform and the heat loss is greater near the southern boundary than it is offshore. Imposing a spatially variable surface cooling with a spatially uniform velocity and stratification allows for other configurations that, while perhaps less realistic than the previous calculation, aid in identifying the important processes that control the net vertical motion resulting from cooling.

Consider first the case of an inflow with uniform horizontal and vertical stratification and a surface cooling that linearly decreases from 1000 W m^{-2} at the southern boundary to zero at the northern boundary (same total heat loss as in the previous case). The geostrophically balanced initial condition and inflow have a zonal velocity that is uniformly sheared in the vertical and constant in the horizontal. The maximum inflow velocity is the same as in the previous calculation, $U = 30$ cm $s^{-1} = H_0 M^2/f_0$, where $H_0 = 500$ is the domain depth and $M^2 = (g/\rho_0)\rho_y = b_y$ is the horizontal stratification. The temperature change across the basin is 0.6°C at all depths, giving $M^2 = 6 \times 10^{-8}$ s^{-2}. This calculation reproduces many of the key features of the previous calculation. The average temperature between days 3 and 10 at 45-m depth is shown in Fig. 4a. The temperature along the offshore boundary is uniform because there is no heat loss there, while the temperature along the southern boundary decreases by approximately 0.4°C. As a result, the total change in density across the channel is less at the outflow than at the inflow, implying a decrease in the vertical shear of the geostrophic velocity at this depth. The average net vertical transport over the region $x = 20$ km to $x = 30$ km is shown in Fig. 5 by the solid line. This profile looks very much like the downwelling in the previous calculation. The net vertical motion is primarily downwelling in the upper ocean with a maximum of 1.11×10^4 $m^3 s^{-1}$ near 100-m depth, decreasing to zero at the surface and at the base of the mixed layer.

Large vertical-scale unstable waves do not develop in these calculations. This differs from the buoyancy-forced frontal calculations of Haine and Marshall (1998), Yoshikawa et al. (2001), and Fox-Kemper et al. (2008), in which baroclinic instabilities grow to dominate the solutions after a few days. There are two important differences between the present calculations and these previous studies. Their fronts were not located on a boundary but were instead in the middle of a wide periodic channel. The current and stratification in the present calculations are specified at the inflow

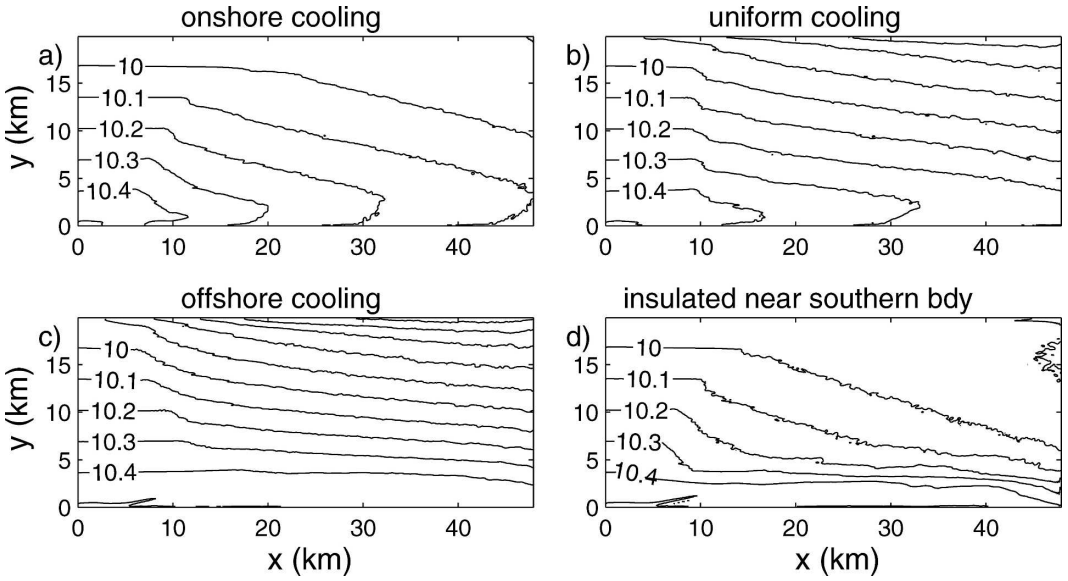

FIG. 4. Temperature at 45-m depth averaged between days 3 and 10 for cases with uniform horizontal velocity at each depth. Heat flux: (a) linearly decays from 1000 W m^{-2} at $y = 0$ to 0 at $y = 20$ km, (b) spatially uniform at 500 W m^{-2}, (c) linearly increases from 0 at $y = 0$ to 1000 W m^{-2} at $y = 20$ km, and (d) linearly decays from 1176 W m^{-2} at $y = 3$ km to 0 at $y = 20$ km.

boundary. This acts to suppress baroclinic instability because the unperturbed, stratified inflow condition is continually advected through the domain. In this sense, along-channel distance in the present model may be thought of as time in the periodic channel models. The boundaries in the present model also tend to suppress baroclinic instability and maintain a strong, well-defined current. While baroclinic instability is often present in separated western boundary currents and open ocean fronts, boundary-trapped currents are generally more stable. This is supported by linear stability theory for flow in a channel (Phillips 1954) and by generally lower values of eddy kinetic energy in altimeter data and high-resolution models for boundary currents near the coast compared to separated boundary currents (e.g., Brachet et al. 2004). Bottom topography near the coasts (not considered here) will also have a stabilizing influence on the boundary current. Thus, the behavior of strong fronts in the absence of baroclinic instability is of general interest and provides a useful complement to the previous open ocean studies.

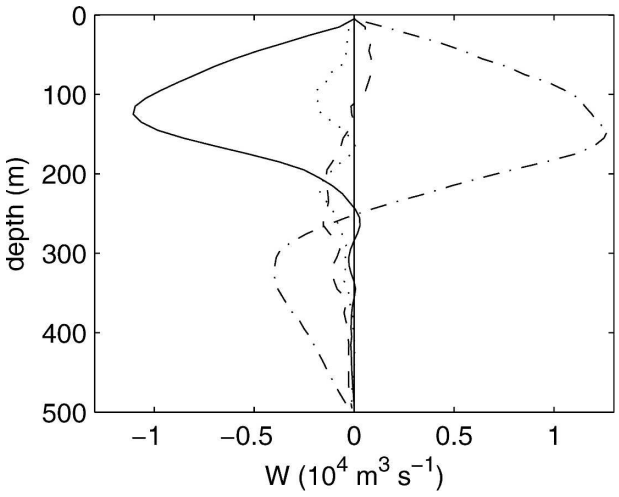

FIG. 5. Vertical mass transport averaged between $x = 20$ km and $x = 30$ km between days 3 and 10. Solid line: cooling decays offshore, dotted–dashed line: cooling increases offshore, dashed line: uniform cooling, dotted line: insulated within 3 km of the southern boundary.

a. Along-channel evolution

The downstream evolution of the along-channel velocity and vertical stratification is indicated by the cross-channel average of the zonal velocity and temperature shown in Fig. 6. The average velocity in the upper 100 m decreases (isotachs slope upward) while the average velocity between approximately 100 and 200 m increases (isotachs slope downward) relative to their inflow values. The change in velocity occurs approximately when the waters at that depth begin to become cooler as a result of mixed layer penetratation. There is a clear correspondence between the decrease in the vertical shear of the zonal velocity and the de-

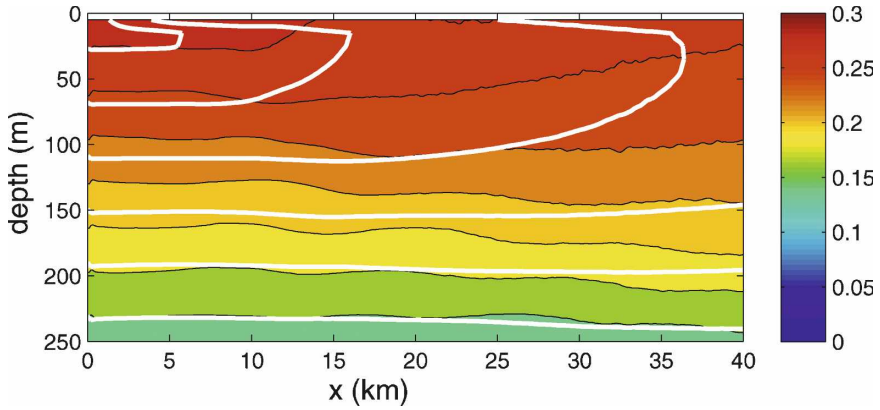

FIG. 6. Meridional average of mean zonal velocity (m s^{-1}, colors) and temperature (white contours, contour interval 0.1°C) as a function of depth and along-channel distance.

crease in the vertical stratification. This supports the interpretation that there is a net vertical mass transport somewhere in the basin that is achieved to maintain a velocity field that is in thermal wind balance with the density field.

The vertical section of the average zonal velocity is shown in Fig. 7a. The development of the no-slip boundary layers is evident along the northern and southern walls. The velocity in the interior, below the mixed layer, is nearly uniform at each depth and close

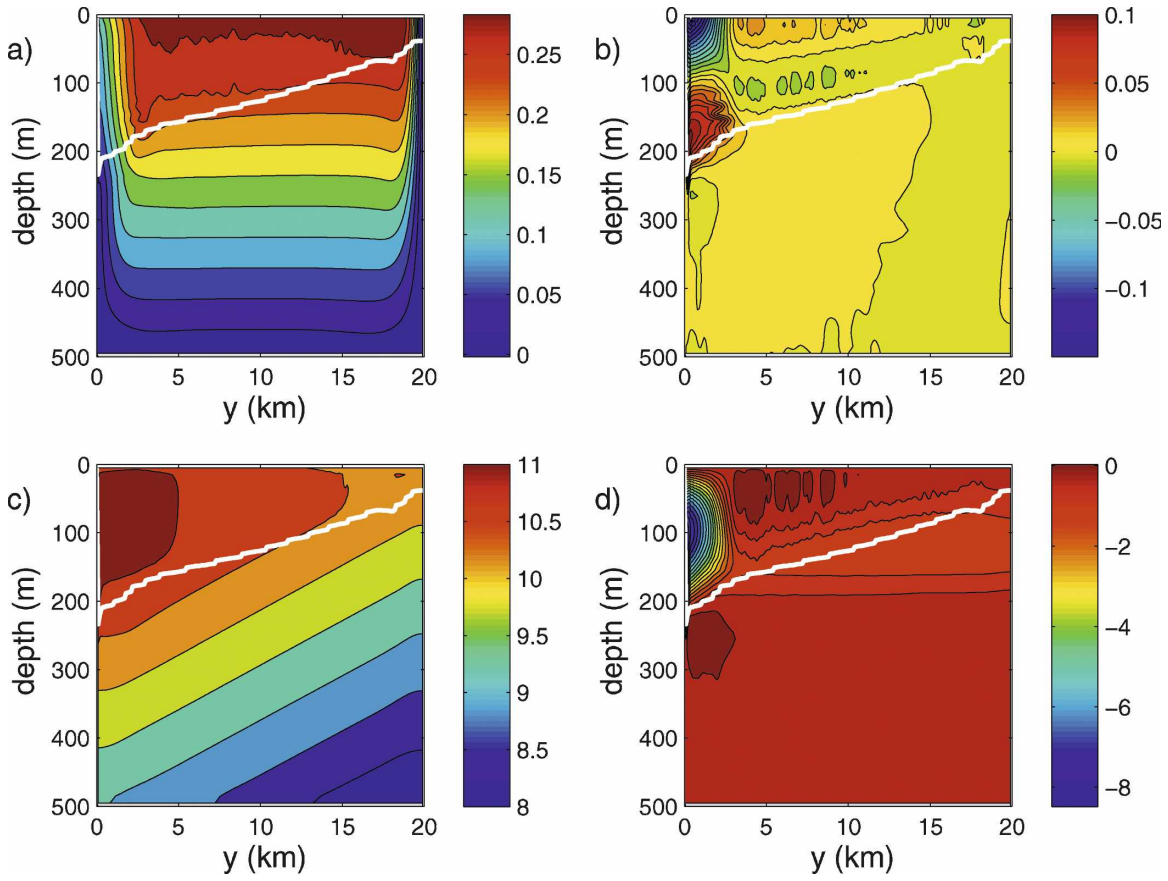

FIG. 7. Vertical section of (a) zonal velocity (m s^{-1}), (b) meridional velocity (m s^{-1}), (c) temperature (°C), and (d) transport streamfunction (10^4 m^3 s^{-1}) averaged between $x = 20$ km and $x = 30$ km between days 3 and 10 for the case with uniform inflow velocity and cooling that decays to zero at $y = 20$ km. The white line indicates the average mixed layer depth.

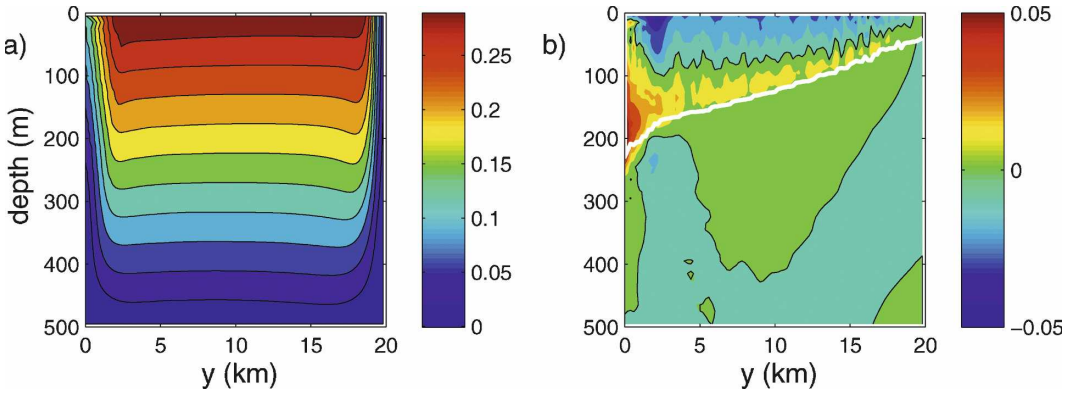

FIG. 8. (a) The mean zonal velocity averaged between $x = 20$ km and $x = 30$ km for a calculation with no surface cooling. (b) The difference in the mean zonal velocity between the calculation with surface cooling (Fig. 7a) and this calculation with no surface forcing (m s^{-1}). The zero contour is in black, and the mixed layer depth from the case with surface cooling is given by the white line.

to the value at the inflow. There has been some increase in the interior velocities in response to the development of the no-slip boundary layers to conserve mass within the domain. Within the mixed layer, however, the velocity near the surface has decreased from its inflow value and the velocity near the base of the mixed layer has increased, particularly in the southern part of the domain. These adjustments make it difficult to distinguish between changes in the zonal velocity resulting from the buoyancy forcing and changes resulting from the development of the no-slip boundary layers. A calculation was carried out that had no surface forcing at all but was otherwise identical to this calculation. The difference in the mean zonal velocity between $x = 20$ km and $x = 30$ km for these two calculations can be attributed solely to the buoyancy forcing. The zonal velocity for this unforced case is shown in Fig. 8a. The development of the no-slip boundary layers, with regions of enhanced zonal velocity adjacent, is evident. However, unlike the buoyancy-forced case, the vertical shear near the surface is nearly the same as it is at depth. The difference in the zonal velocity between the buoyancy-forced case and this unforced case is shown in Fig. 8b. The depth of the mixed layer for the case with surface cooling is indicated by the bold white line. The zero contour is black. Most of the velocity change due to buoyancy forcing is found within the mixed layer. The zonal velocity is decreased in the upper portion of the mixed layer and increased near the base of the mixed layer, resulting in weaker vertical shear throughout most of the mixed layer. Very close to the southern boundary, the zonal velocity is increased throughout the mixed layer. This is different from the behavior in the interior and is due to the development of a very narrow boundary layer, discussed further below.

b. *Cross-channel circulation*

The cross-channel velocity shows the same two cells that were found for the case with uniform cooling and spatially variable along-channel velocity (Fig. 7b). In the interior, the cross-channel flow is of $O(1\ \text{cm s}^{-1})$ and restratifying. This sense of circulation is opposite to what would be expected for a geostrophically balanced flow, in which the upper mixed layer flow would be toward the southern boundary and the deep mixed layer would be away from the boundary (Spall and Pickart 2001). Such a geostrophic flow is found if the viscosity and diffusivity are increased by a factor of 5 (discussed further in the next section). The restratifying flow is a result of small-scale instabilities in the mixed layer, as discussed further below.

The vertical section of temperature shows both the vertical extent of the mixed layer and the decrease in lateral density gradient compared to the inflow conditions. There is a thin layer of negative temperature gradient near the surface, consistent with the nonhydrostatic physics and cooling at the surface. The well-mixed region extends down to 200 m along the southern boundary and recedes toward the surface on the northern side of the channel, where the surface cooling goes to zero. The temperature change across the channel at the surface at the inflow is 0.6°C, while at this section it is only 0.2°C. It is this reduction in the horizontal density gradient, and the resulting reduction in the vertical shear of the along-channel velocity, that requires net vertical motion to maintain geostrophic balance. Most of the temperature change takes place well outside the viscous boundary layers, in the interior of the channel.

The cross-channel overturning streamfunction ψ

shows two cells analogous to those found in the case with uniform cooling (Fig. 7d). The finding that the streamfunction does not go to zero at the northern boundary indicates that there is a net downwelling at that depth (as in Fig. 5). The streamfunction contours are level below the mixed layer, verifying that essentially all of the vertical motion is contained within the mixed layer. This isolation of the vertical motion to the mixed layer distinguishes this process from vertical motions within the stratified boundary layer of width proportional to the internal deformation radius discussed by Barcilon and Pedlosky (1967). The interior cross-channel flow results in downwelling within the mixed layer (the downward-sloping contours shallower than the mixed layer) as a result of the decreasing cross-channel velocity as the mixed layer shallows.

The cell near the southern boundary has strong upwelling within several kilometers of the boundary and intense downwelling within 100 m of the wall (one grid). This cell is a direct result of the lateral shear found in the no-slip boundary layer. Far from the wall, the relative vorticity is much smaller than f and the along-channel pressure gradient is balanced largely by a weak cross-channel geostrophic flow. However, within a few kilometers of the boundary, the horizontal shear of the along-channel flow is sufficiently large such that the relative vorticity is $O(-f_0)$, so that the absolute vorticity becomes much smaller than f_0 (but not less than 0). The nonlinear momentum balance, appropriate for this region, becomes $(f_0 - u_y)v \approx P_x$. The pressure gradient is maintained by the surface cooling. As the absolute vorticity becomes small, the meridional velocity must increase to balance the pressure gradient. This results in an increasingly large cross-channel velocity as the wall is approached. This occurs all along the channel, so the only way in which the mass can be balanced is to upwell water from the deep mixed layer. The along-channel pressure gradient changes sign at the midpoint of the mixed layer, so that the same situation arises in the lower mixed layer but with opposite sign, supporting flow away from the wall. A similar cell is found with increased viscosity and diffusivity, even though mixed layer instabilities are suppressed; thus, it is not a manifestation of mixed layer instabilities with increased magnitude due to the presence of anticyclonic shear. A different balance, in which lateral viscosity is important, is found very near the wall where $v \to 0$, as discussed in the subsection on the nonhydrostatic boundary layer.

A scaling estimate for the strength of this nonlinear recirculation cell can be derived from the two-dimensional depth-meridional streamfunction equation presented by Hoskins (1975) and discussed recently in terms of submesoscale variability in the mixed layer by Thomas et al. (2008). The ageostrophic, cross-channel flow forced by cooling may be expressed in terms of the streamfunction ψ as

$$F^2 \frac{\partial^2 \psi}{\partial z^2} + 2M^2 \frac{\partial^2 \psi}{\partial z \partial y} + N^2 \frac{\partial^2 \psi}{\partial y^2} = -2Q, \qquad (1)$$

where $F^2 = f_0(f_0 - u_{gy})$, $Q = -\mathbf{u}_{gy} \times \nabla b$, and u_g is the geostrophic zonal velocity. For the present problem, $Q \approx u_{gy} b_x$. For horizontal length scales larger than the vertical length scale, the third term on the left-hand side can be neglected. At the depth for which the streamfunction is a maximum, the second term, proportional to ψ_z, can also be neglected. A scaling for the maximum streamfunction $\psi_{\max}$ can then be derived by balancing the first term on the left-hand side with the forcing

$$\psi_{\max} = \frac{u_{gy} b_x H^2}{f_0(f_0 - u_{gy})}. \qquad (2)$$

This estimate can be simplified for the present case, where the horizontal advection of density is balanced by surface cooling, so that $u_g b_x \approx B/H$, where B is the surface buoyancy flux. Combining with (2), the overturning streamfunction scales as

$$\psi_{\max} = \frac{BH}{Lf_0^2}, \qquad (3)$$

where it has been assumed that the geostrophic velocity varies on a horizontal length scale L and that, for simplicity, $f_0 - u_{gy} = O(f_0)$. The meridional velocity scales as $V = \psi_{\max}/H = B/Lf_0^2$. For the present problem, $B = O(10^{-6}\ \mathrm{m^2\,s^{-3}})$, $f_0 = 10^{-4}\ \mathrm{s^{-1}}$, and $L = O(10^3\ \mathrm{m})$, giving $V = 10^{-1}\ \mathrm{m\,s^{-1}}$, in general agreement with the numerical model results. This scaling demonstrates that the nonlinear recirculation cell is driven directly by the surface cooling and relies critically on the anticyclonic shear layer of width L. The width of this no-slip boundary layer is roughly determined by a balance between zonal advection of zonal momentum and lateral viscosity, resulting in a boundary layer width that grows with distance downstream as $x^{1/2}$. The value of 10^3 m used for this scaling is only approximate and was diagnosed from the model results.

c. Symmetric instabilities

These time- and space-averaged quantities smooth over what is a highly temporally and spatially variable flow (Fig. 9). In the interior, more than 2–3 km from

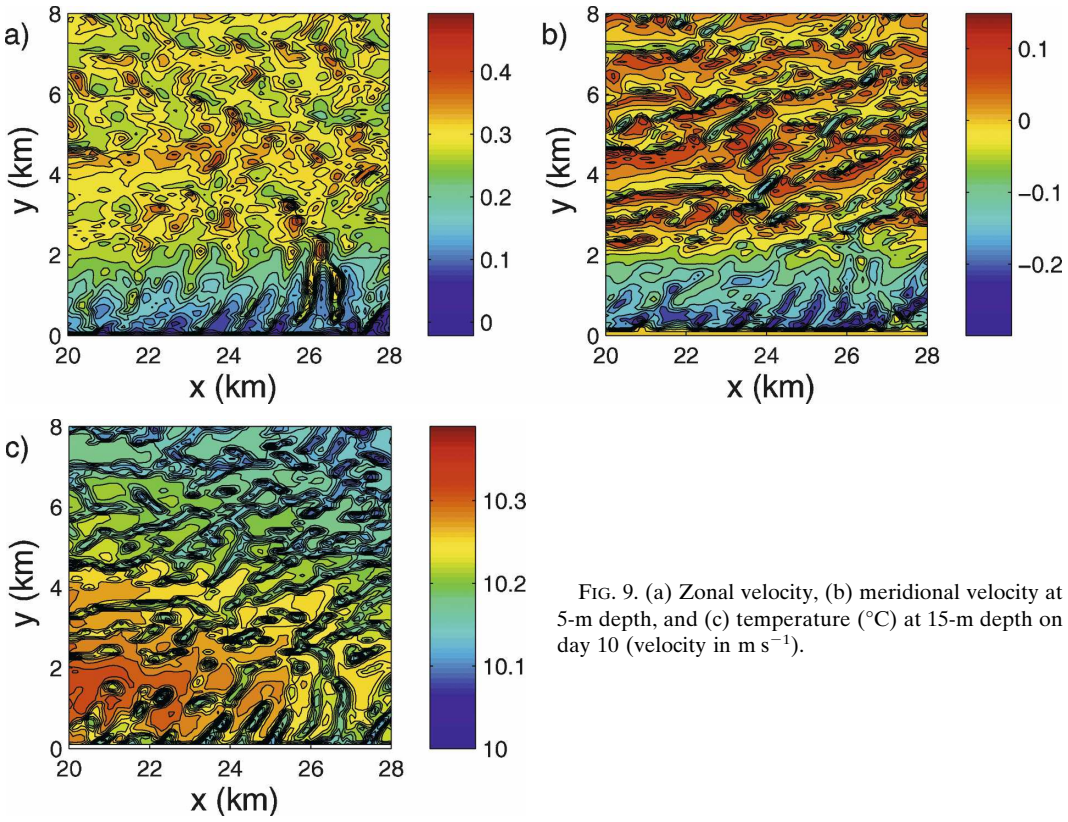

FIG. 9. (a) Zonal velocity, (b) meridional velocity at 5-m depth, and (c) temperature (°C) at 15-m depth on day 10 (velocity in m s^{-1}).

the southern boundary, the zonal velocity varies by $O(10\ \text{cm s}^{-1})$ on horizontal scales of $O(1\ \text{km})$. Near the boundary, the no-slip boundary layer is punctuated by along-boundary perturbations of zonal scale $O(1\ \text{km})$ that span the region of decreasing zonal flow. In the interior, the meridional velocity varies with similar magnitude, but it is coherent over length scales of several kilometers in the zonal direction and less than 1 km in the meridional direction. The interior flow is dominated by narrow, zonally elongated convergent and divergent filaments. Near the wall, the meridional velocity takes on the longer meridional length scales of the no-slip boundary layer and short zonal length scales of less than 1 km. The meridional flow near the boundary is strongly southward, toward the boundary. It is apparent that the nature of the mixed layer instability is different in the interior, where the perturbations take the structure of multiple zonal jets with small meridional scale, compared to within the no-slip boundary layer, where the perturbations are oriented more perpendicular to the boundary and span the boundary layer width. The temperature field at 15-m depth is dominated by narrow bands of dense water below the convergence zones in the surface layer (Fig. 9c). The vertical velocity in these regions is downward, bringing down the more dense waters with negative potential vorticity formed at the surface. Weaker upwelling regions are found between these dense plumes, carrying warmer, higher potential vorticity waters toward the surface. A similar vertical flux of potential vorticity is carried by small-scale ageostrophic cells for cases of wind forcing along baroclinic flows, as discussed by Thomas (2005).

These small-scale features are interpreted as being due to symmetric instability. Stone (1966) showed that symmetric instability is expected when the Richardson number, defined as $\text{Ri} = N^2 f^2 / M^4$, is within the range $0.25 < \text{Ri} < 0.9$. The average horizontal and vertical stratification was calculated from the surface to the depth, $\int\int \overline{w^2} dx\ dy = 0.1\ (\int\int \overline{w^2} dx\ dy)_{\text{max}}$, where the overbar indicates a time average and the subscript "max" indicates the maximum value of the spatially averaged variance in the vertical velocity. This maximum variance is found near the middepth of the mixed layer. This diagnostic identifies the portion of the water column where the instabilities are most active in a manner that is not directly dependent on N^2, although the depth range of the instabilities is very close to the mixed layer depth. The factor of 0.1 is somewhat arbitrary, although similar results are found for any value that identifies that part of the water column with most

of the variance. The resulting Richardson number within the region in Fig. 9 is 0.47, well within the range appropriate for symmetric instability. A model simulation with a mixed layer 150 m deep in the initial and inflow conditions, but with no surface forcing, does not produce these strong, small-scale convergent regions, indicating that it is the active surface forcing—not the presence of a mixed layer—that is responsible. The potential vorticity near the surface is negative in the buoyancy-forced calculation, a feature conducive to symmetric instability. In addition, a calculation with surface cooling and the viscosity increased by a factor of 5 does not form these features. This is consistent with symmetric instability because it grows mainly at the expense of the kinetic energy of the mean flow via eddy momentum fluxes (Stone 1966), and so it is more easily suppressed by mixing of momentum than it is by mixing of density. Unlike the open ocean frontal calculations by Haine and Marshall (1998) and Yoshikawa et al. (2001), the symmetric instabilities are present throughout the calculation because baroclinic instability does not develop. It is also noted that due to the nonperiodic nature of the domain, there is no cascade toward larger scales, as found in the periodic channel calculations of Fox-Kemper et al. (2008).

d. The nonhydrostatic layer

There is very intense downwelling directly next to the southern boundary. The width of this downwelling layer can be estimated following the approach of Stewartson (1957), who found that there are two narrow boundary layers required to transition a region of interior flow driven by stress at the surface and bottom to that of an adjacent flow driven at a different speed. A boundary layer of width $E^{1/4}$ exists to allow the geostrophic flow parallel to the boundary to smoothly transition from one regime to the other, where $E = A/f_0L^2$ is the horizontal Ekman number, A is the horizontal viscosity, and L is a horizontal length scale. However, this transitional layer cannot support the vertical mass transport that is required to match the upper and lower Ekman layers. This is achieved in a narrower nonhydrostatic boundary layer of nondimensional width $E^{1/3}$ or dimensional width $(AH/f_0)^{1/3}$, where H is a vertical length scale. While the $E^{1/4}$ layer does not exist for the present problem, in which the forcing is due to an along-boundary pressure gradient and not surface and bottom Ekman layers, the $E^{1/3}$ layer that carries the vertical mass transport does. The zonal pressure gradient, which was not considered in the original solution by Stewartson, does not alter the width of this boundary layer. For the values used here ($f_0 = 10^{-4}$ s^{-1}, $A = 1$ m^2 s^{-1}, $H = 100$ m), the horizontal scale of the downwelling region is predicted to be $O(100$ m).

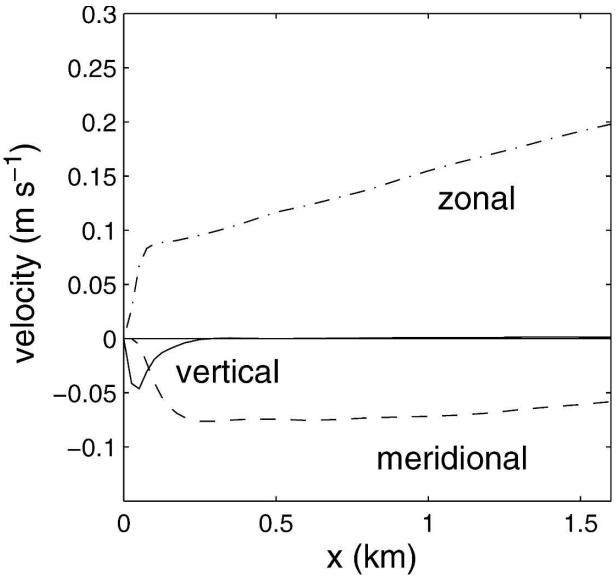

FIG. 10. The mean horizontal and vertical velocities near the southern boundary at 45-m depth from the calculation with enhanced meridional resolution near the boundary.

The downwelling near the wall in the model is contained mostly within one grid cell of the boundary, so it is not well resolved with the standard grid. An identical calculation was carried out with the meridional resolution increased to 25 m between 0 and 200 m and 50 m between 200 and 400 m from the boundary. The net vertical transport in this case is very similar to the standard resolution case, 1.24×10^4 m^3 s^{-1} compared to 1.11×10^4 m^3 s^{-1}. The mean zonal, meridional, and vertical velocities between $x = 20$ km and $x = 30$ km near the southern boundary at 45-m depth are shown in Fig. 10. The downwelling is still concentrated within 100 m of the wall, so the horizontal scale of this downwelling region, while only marginally resolved with the standard grid, is $O(100$ m), consistent with that predicted by the $E^{1/3}$ Stewartson layer. Linear interpolation of the vertical transport indicates that 80% of the total downwelling occurs within 107 m of the boundary. A calculation with the horizontal viscosity increased to 8 m^2 s^{-1} results in 80% of the downwelling occurring within 204 m of the boundary, in close agreement with the expected doubling of the boundary layer width for a factor-of-8 increase in viscosity.

The meridional velocity rapidly decreases from $O(0.1$ m s$^{-1})$ to zero within this narrow layer. Most of this convergence of the meridional flow is taken up by downwelling, so the mass balance is nearly two-dimensional here. The second derivative of the zonal

velocity u_{yy} becomes very large near the wall, as required for the viscous term to balance the flow toward the wall in the zonal momentum equation. This boundary layer results in a zonal velocity at the edge of the nonhydrostatic layer that is larger than would be found in the no-slip boundary layer in the absence of buoyancy forcing. This is evident in Fig. 7a by larger zonal velocity within the mixed layer near the southern boundary compared to the no-slip layer near the northern boundary or below the mixed layer at the southern boundary (both locations where the buoyancy forcing is weak). A detailed analysis of this boundary layer in the linear limit by Pedlosky (2009) verifies that the horizontal scale of the downwelling region, and the abrupt gradient in the along-boundary flow, scales as $E^{1/3}$. His analysis shows that it is the weak vertical stratification that is key to the existence of this narrow nonhydrostatic layer whose function is to bring the cross-channel geostrophic flow to zero at the wall.

e. Cooling distribution

This calculation with spatially variable cooling shows many similarities with the uniform cooling case and spatially variable along-channel flow. The advantage of the spatially variable cooling and uniform velocity is that other configurations can be employed that assist in our understanding of what controls the net downwelling. A case with spatially uniform cooling of 500 W m^{-2} and uniform horizontal and vertical stratification results in density changes along both the southern and northern boundaries (Fig. 4b). The magnitude of the change in temperature along each boundary is similar, so that the net change in density across the channel at the outflow is very similar to the net change in density at the inflow, even though the density itself has increased. The net vertical mass transport between 20 and 30 km is very small (Fig. 5). Even though there is a mixed layer of O(100 m) depth, and mixed layer instabilities form and drive a restratifying cross-channel circulation, they do not drive a net vertical motion when integrated across the basin. A revealing calculation is obtained with a heat loss that is zero at the southern boundary and increases linearly to 1000 W m^{-2} at the northern boundary. Now, the temperature is nearly constant along the southern boundary but decreases by approximately 0.4°C along the northern boundary (Fig. 4c). The net vertical motion in this case is upward at about the same amplitude as the downwelling found in the case with cooling enhanced along the southern boundary (Fig. 5).

A final calculation was carried out in which the heat loss increased from zero at the northern boundary to 1176 W m^{-2} at 3 km from the southern boundary and was zero within 3 km of the southern boundary. The sea surface temperature is constant along the northern boundary but is now also nearly constant along the southern boundary (Fig. 4d). Because there is no heat loss there, there is no means to support a strong pressure gradient and the along-channel velocity simply advects the isotherms downstream. The strong meridional cell adjacent to the southern boundary is not present in this case, again demonstrating its connection to the pressure gradient near the boundary. The net vertical motion is also very weak (Fig. 5). A similar sensitivity to surface insulation within 200 km of the boundary was found by Spall and Pickart (2001) for the basin-scale overturning circulation in a non-eddy-resolving climate model. The present results suggest that this process will remain important for the basin-scale thermohaline circulation, even when the lack of convection is limited to within a few kilometers of the boundary. This result is also consistent with the modeling study of Walin et al. (2004), in which a baroclinic current was cooled and formed a barotropic boundary current yet resulted in no net downwelling. The form of their surface forcing resulted in no heat loss adjacent to the boundary and was thus unable to support a pressure gradient, or downwelling, along the boundary.

The two calculations here that do not have a change in the density gradient across the channel both have the interior ageostrophic overturning cell driven by the mixed layer instabilities, yet neither has any appreciable net vertical motion in the basin, demonstrating that these cells play no direct role in the net sinking in the basin. The strong cell near the southern boundary is also found in the case with uniform cooling, and there is no equivalent cell near the northern boundary (because the relative vorticity is positive there), yet there is no net vertical motion, demonstrating that this cell is not a significant component of the downwelling. Sinking is achieved when the density within the mixed layer increases along a boundary in the direction of Kelvin wave propagation; upwelling results when it decreases in the direction of Kelvin wave propagation.

4. Parameter dependencies

The results in the previous section isolate the pressure gradient along the boundary as the key feature that controls net vertical motion. The pressure gradient on the boundary is related to the mixed layer depth and the density gradient along the boundary through the hydrostatic relation. Each of these calculations had the same net surface heat loss yet demonstrated completely different net vertical motions, clearly demonstrating

that there is no direct relationship between heat loss and downwelling. The key to understanding the downwelling is to understand what controls the pressure gradient along the boundary. A simple model of the temperature within the mixed layer is now formulated to provide a framework with which to understand and predict how the buoyancy-forced downwelling will vary with environmental parameters.

For simplicity, it will be assumed that the pressure does not vary along the offshore side of the boundary current. For cyclonic boundary currents that encircle marginal seas subject to buoyancy forcing, this is roughly consistent with having the offshore edge of the boundary current being defined by an isotherm. The net downwelling is then determined by the lateral large-scale flow into the very narrow nonhydrostatic layer adjacent to the boundary. An important assumption here is that the boundary layer exists to satisfy the no-normal flow boundary condition and conserve mass and that the pressure gradient is set by the flow in the boundary current just outside the narrow boundary layer. It is also assumed that all of the transport toward the boundary layer downwells within the boundary layer. This is in close agreement with the numerical results and is also supported by the linear theory of Pedlosky (2009).

Consider the buoyancy balance near the southern boundary within the mixed layer but outside the nonhydrostatic layer of width $E^{1/3}$. If the along-channel velocity at the base of the mixed layer is U, the mixed layer depth is h, the mixed layer buoyancy is $b = -g\rho/\rho_0$, and the surface buoyancy flux $B = \alpha g Q/\rho_0^2 C_p$, then the density equation within the mixed layer may be written as

$$Ub_x = -\frac{B}{h}, \tag{4}$$

where α is the thermal expansion coefficient; g is the gravitational acceleration; C_p is the specific heat of seawater; and the variables U, b, and h are functions of downstream distance x only. This is a balance between the along-boundary advection of buoyancy and surface cooling. Note that if the vertical shear of the horizontal velocity within the mixed layer is in thermal wind balance, then the buoyancy is not advected by the baroclinic shear components of the velocity, and so the buoyancy budget only depends on the velocity at the base of the mixed layer. If it is assumed that the mixed layer is an unstratified layer overlaying a uniformly stratified region below, the depth of the mixed layer can then be related to the buoyancy as

$$h = -\frac{b}{N^2}, \tag{5}$$

where $N^2 = b_z$ is the Brunt–Väisälä frequency and b is taken to be relative to the surface buoyancy in the absence of any cooling ($h = 0$ when $b = 0$). Combining with (4), the buoyancy gradient in the along-channel direction can be written as

$$b_x = \left(\frac{BN^2}{2Ux}\right)^{1/2}. \tag{6}$$

The downstream buoyancy gradient increases with increasing cooling, as expected. However, the buoyancy gradient also depends on the along-channel velocity because the balance is between horizontal advection of buoyancy and surface cooling. The dependence on stratification enters because the mixed layer will be shallower for stronger underlying stratification, and the buoyancy change will be larger for a shallower mixed layer.

Spall and Pickart (2001) considered the geostrophic flow within a mixed layer subject to cooling and found that for a density that is increasing downstream, the flow will be toward the boundary in the upper half of the mixed layer and away from the boundary in the lower half of the mixed layer. This gives a maximum downwelling at the middepth of the mixed layer, per unit along boundary distance, of

$$W = -\frac{b_x h^2}{8f_0}. \tag{7}$$

This expression was found to compare well with a series of low-resolution, basin-scale, wind- and buoyancy-driven general circulation models.

If the mixed layer depth were known, the downwelling rate could be derived from (4) and (7) to be

$$W = \frac{Bh}{8f_0 U}. \tag{8}$$

It is clear from (5) that the mixed layer depth will increase downstream as the boundary current is cooled and the buoyancy decreases. Equation (7) may be combined with (5) and (6) to provide an estimate of the downwelling per along-boundary distance varies with downstream position as

$$W = \frac{1}{4f_0}\left(\frac{B^3 x}{2N^2 U^3}\right)^{1/2}. \tag{9}$$

Although this expression is more complicated than (8), it is also more revealing regarding the competing effects that influence net downwelling. The downwelling increases with increasing cooling, as expected, but it also increases with increasing distance, decreasing

TABLE 1. Summary of model runs with key parameters and the maximum average downwelling rate (W) between $x = 20$ km and $x = 30$ km.

Run	Q (W m^{-2})	f_0 (10^{-4} s^{-1})	H_0 (m)	M^2 (10^{-8} s^{-2})	N^2 (10^{-6} s^{-2})	W (10^4 m^3 s^{-1})
1	1000	1	500	6	4.8	1.04
2	1000	1	500	9	4.8	0.50
3	1000	1	500	3	4.8	2.26
4	1000	0.5	500	6	4.8	0.95
5	1000	2	500	6	4.8	1.37
6	500	1	500	6	4.8	0.37
7	1500	1	500	6	4.8	1.70
8	2000	1	500	6	4.8	2.75
9	1000	1	500	6	2.4	1.67
10	1000	1	500	6	7.2	0.69
11	1000	1	1000	2.4	1.9	2.91

velocity, decreasing stratification, and decreasing Coriolis parameter. Downwelling depends on distance because the mixed layer depth increases with distance downstream. Less downwelling is found for stronger boundary currents because the pressure gradient is less due to stronger horizontal advection balancing the surface cooling, but it is also due to the fact that a stronger horizontal advection limits the depth of mixing [Eq. (4)]. The downwelling also increases with decreasing stratification because the mixed layer will penetrate further for the same cooling rate. The increasing downwelling with decreasing Coriolis parameter is simply due to the geostrophic balance resulting in more flow toward the boundary to balance a given pressure gradient.

A series of model calculations was carried out to test the parameter dependencies predicted by (9). The model was forced with uniform horizontal and vertical stratification and a heat loss that was maximum at the southern boundary and linearly decreased to zero at the northern boundary. The magnitude of the surface cooling, vertical stratification, along-channel geostrophic flow, and Coriolis parameter were each varied, as summarized in Table 1. Each of these model calculations was carried out with 200-m horizontal resolution and 10-m vertical resolution; however, the circulation features are very similar to the previously discussed calculation with higher resolution. The maximum net downwelling per unit along boundary distance is also similar (1.11 m^2 s^{-1} for the high-resolution calculation and 1.04 m^2 s^{-1} for the low-resolution calculation). The maximum downwelling rate was calculated, as in Fig. 5, for each of these calculations and is compared with the theory in Fig. 11. The velocity scale used in (9) has been taken to be proportional to the surface geostrophic velocity at the inflow, $U = cH_0 M^2/f_0$, where the constant $c = 0.43$ produces a least squares fit line to the data with slope 1. It is expected that $c < 1$ because the velocity decreases within the no-slip boundary layer, which is much wider than the downwelling layer. Nonetheless, the geostrophic scaling allows for a systematic means to estimate the influence of the horizontal velocity on the downwelling and makes clear the dependence on the controlling parameters M^2 and f_0.

The agreement between the downwelling diagnosed from the model and that predicted by the simple theory is quite good. The central calculation is indicated by the square (low resolution) and star (high resolution)—the two are nearly indistinguishable on this scale. It is interesting that all but three of these calculations are sub-

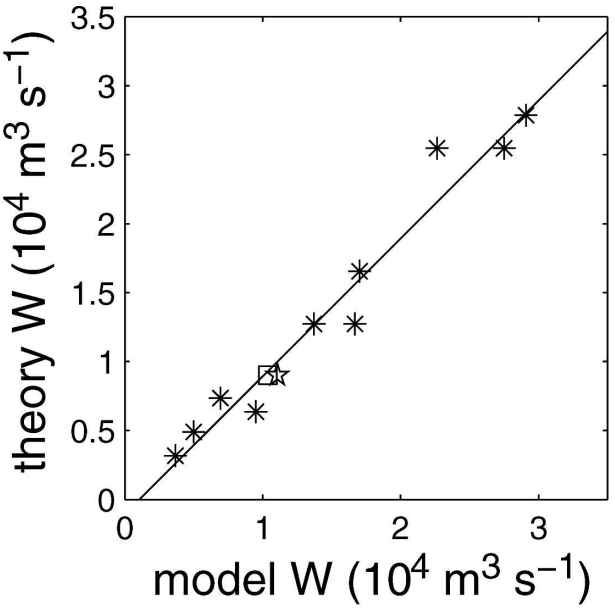

FIG. 11. Comparison of the net downwelling between $x = 20$ km and $x = 30$ km calculated from the model and that predicted by theory (9) (see Table 1 for a summary). The square marks the central calculation and the star marks a calculation with the same parameter settings and a horizontal resolution of 100 m.

ject to the same heat loss at the surface yet the net downwelling varies by a factor of 6.

It is somewhat counterintuitive that the simple theory (9) indicates that the total downwelling does not depend on the offshore extent of the boundary current or the amplitude or pattern of cooling away from this near-boundary region. To demonstrate this independence, the model was run with a maximum heat loss of 1000 W m^{-2} at the southern boundary that linearly decreased to zero at the northern boundary in a channel 40 km wide, twice as wide as in the standard case. The horizontal velocity, horizontal stratification, and vertical stratification were the same as the standard case, but due to the wider domain, the total heat loss was twice as large. The total net downwelling in this case was 1.08×10^4 m^3 s^{-1}, essentially the same as for the 20-km-wide channel. The downwelling is independent of the current width provided that the current transports enough heat to balance the surface cooling and maintain the along-boundary baroclinic pressure gradient.

The net downwelling does show some dependence on the lateral boundary condition for velocity. Using free-slip boundary conditions and the standard forcing, the downwelling rate is 0.74×10^4 m^3 s^{-1}, almost 30% less than with no-slip boundary conditions. The ageostrophic cell near the boundary is absent because there is no strong anticyclonic relative vorticity near the wall with the absence of the no-slip layer. This indicates that this nonlinear aspect of the calculation is not necessary to support downwelling, but also suggests that the details of the near boundary region are important for the quantitative downwelling. It is not clear from this calculation if the lower downwelling rate is due to a larger horizontal velocity near the boundary, which, from (9), is expected to result in weaker downwelling, or if there is some more fundamental difference associated with the free-slip boundary condition and the nonhydrostatic layer and its transition to the interior flow.

It does not appear to be necessary to resolve the nonhydrostatic physics and convective plumes explicitly. A hydrostatic calculation with horizontal viscosity and diffusivity increased to 5 m^2 s^{-1} and, with vertical convection parameterized by increasing the vertical diffusivity to 1000 m^2 s^{-1} for unstable profiles, results in a net downwelling of 1.10×10^4 m^3 s^{-1}, close to the standard calculation. The subgrid-scale mixing is sufficiently large that the symmetric instabilities are suppressed, but all other aspects of the zonally averaged flow are similar to the nonhydrostatic result. The density within the mixed layer is essentially uniform with depth. The mean cross-channel flow in the interior is now toward the boundary in the upper mixed layer and away from the boundary in the lower mixed layer, as expected from geostrophy (Spall and Pickart 2001). The ageostrophic cell near the southern boundary is also found, again supporting the interpretation that this is not resulting from an instability of the mixed layer.

The underlying circulation that redistributes mass in the vertical is more clearly revealed by considering a hydrostatic calculation with free-slip boundary conditions and increased viscosity and diffusivity of 5 m^2 s^{-1}. This suppresses the strong nonlinear recirculation gyre near the boundary in addition to the symmetric instabilities in the interior. The resulting net downwelling rate is 0.75×10^4 m^3 s^{-1}, very close to that found with free-slip boundary conditions, nonhydrostatic physics, and low visosity and diffusivity. The along-channel velocity is a maximum adjacent to the southern boundary because the no-slip boundary layer is no longer present (Fig. 12a). However, the cross-channel velocity is now dominated by flow toward the southern boundary over the upper mixed layer and flow away from the boundary in the deep mixed layer and just below the mixed layer. Note that the magnitude of this cross-channel flow is less than that found when symmetric instabilities are present, but it is just what is required to provide the net downwelling rate of $O(1\ m^2\ s^{-1})$ along the boundary. The magnitude of the meridional velocity increases toward the boundary in both the upper and lower mixed layer. The vertical velocity, as implied by the streamfunction in Fig. 12d, is near zero over most of the interior of the basin. This indicates that the change in v toward the southern boundary is gained largely at the expense of the along-channel velocity, not by upwelling and/or downwelling in the interior. The downwelling is localized primarily within one grid cell of the southern boundary, although there is weaker downwelling within approximately 1 km of the southern boundary. This profile is very similar to that predicted by the linear theory of Pedlosky (2009). This calculation demonstrates that the redistribution of mass in the vertical is achieved by a geostrophic flow toward the boundary in the upper mixed layer, downwelling very close to the boundary, and a return flow away from the boundary below the mixed layer. Thus, while the acceleration at the base of the mixed layer is physically very close to the deceleration at the surface, the water parcels had to make a long traverse all the way to the narrow boundary layer to sink to the deeper depth.

5. Conclusions

The physics controlling the net downwelling resulting from surface cooling are explored using a high-

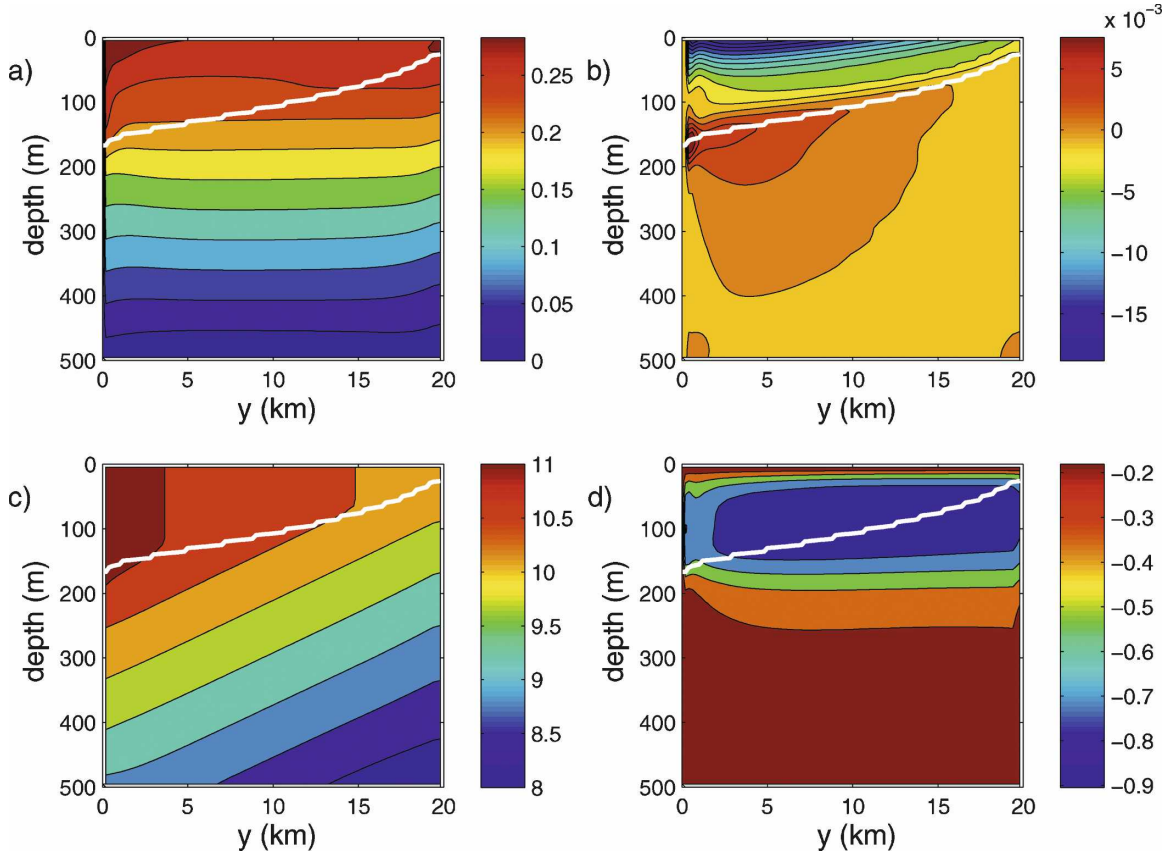

FIG. 12. Vertical section of (a) zonal velocity (m s^{-1}); (b) meridional velocity (m s^{-1}); (c) temperature (°C); (d) transport streamfunction (10^4 m^3 s^{-1}) averaged between $x = 20$ km and $x = 30$ km between days 3 and 10 for the case with hydrostatic physics, free-slip boundary conditions, and viscosity and diffusivity of 5 m^2 s^{-1}. The inflow velocity is uniform, and the surface cooling decays from 1000 W m^{-2} at $y = 0$ to zero at $y = 20$ km. The white line indicates the average mixed layer depth.

resolution, nonhydrostatic ocean model and a simple advective model of the mixed layer. The focus is placed on the types of ageostrophic motions that are generated by cooling in the presence of strong horizontal advection and boundaries and on the net vertical transport of mass. Previous studies have shown that buoyancy loss in the interior of ocean basins results in a vertical transport of heat but little vertical mass transport (Send and Marshall 1995; Marotzke and Scott 1999; Spall 2003, 2004). The small-scale regions of intense downwelling within convective plumes are balanced by weaker upwelling in the surrounding areas, such that the area integral of the vertical velocity approaches zero when averaged over length scales large compared to the internal deformation radius.

The introduction of a boundary and horizontal advection can result in a net downwelling. The crucial element to support downwelling is the maintenance of a pressure gradient along the boundary. For weak diapycnal mixing in the ocean interior, the pressure gradient along the boundary is isolated within the mixed layer. The lateral advection of heat by the boundary current balances surface cooling, resulting in a density change and thus a pressure gradient along the boundary within the mixed layer. If the geostrophic velocity associated with this pressure gradient is oriented into the boundary at the surface, then there is a net downwelling. If it is oriented away from the boundary, then there is a net upwelling. Both are possible equilibrium states for a boundary current subject to cooling, depending on which side of the boundary current the boundary is located. For cyclonic boundary currents that flow in the same direction as Kelvin wave propagation, as are typically found in marginal seas subject to net buoyancy loss at the surface, the net vertical motion is downward. Thus, the physics described here are relevant to the downwelling limb of the thermohaline circulation that is forced by surface cooling. The mass transport is carried downward in a narrow nonhydrostatic boundary layer analogous to the classical $E^{1/3}$

Stewartson layer, where E is the Ekman number. The vertical redistribution of mass required by geostrophy in the interior is achieved by an upper ocean geostrophic flow toward the boundary, downwelling within the narrow Stewartson layer, and a geostrophic flow away from the boundary at depth. Calculations with a sloping bottom indicate that the Stewartson layer is replaced by a bottom Ekman layer, but the net downwelling remains very similar.

A simple model of the mixed layer depth and density near the boundary is derived and used to predict the net downwelling resulting from buoyancy loss at the surface. The model shows that the net downwelling depends on the surface heat loss, but it is also dependent on the strength of the boundary current, the vertical stratification below the mixed layer, the mixed layer depth, and the Coriolis parameter. The net vertical transport, diagnosed from a series of numerical model calculations in which each of these parameters is varied, compares well with that predicted by the theory.

The success of the geostrophic mixed layer model in predicting the net downwelling found in the nonhydrostatic model suggests that the details of the narrow downwelling regions or of convective plumes do not need to be resolved to represent the large-scale impacts of the downwelling limb of the thermohaline circulation that is forced by surface buoyancy loss. However, the details of the geostrophic flow near the boundary, in particular the mixed layer depth and the horizontal velocity, do need to be represented properly. These physics highlight the importance of mixing processes near the boundary and the possibility that narrow regions of ice cover or freshwater discharge near the coast, which will largely insulate the ocean to surface cooling, can have a large impact on the overturning circulation at high latitudes. These results also suggest that low-resolution climate models, which will typically underestimate the horizontal velocity in strong boundary currents, will overestimate the downwelling forced by surface cooling. This is consistent with the increasing importance of the horizontal gyre, and decreasing importance of the overturning gyre, for the meridional heat transport found by Fanning and Weaver (1997) as the horizontal resolution was increased in a coupled climate model. Any parameterization aimed at improving the downwelling in low-resolution models must focus on improving the explicitly resolved geostrophic velocities near the boundary.

Acknowledgments. This work was supported by NSF Grants OCE-0423975 and OCE-0726339. This work has benefitted from many discussions with Joseph Pedlosky and Leif Thomas.

REFERENCES

Barcilon, V., and J. Pedlosky, 1967: A unified theory of homogeneous and stratified rotating fluids. *J. Fluid Mech.,* **29,** 609–621.

Brachet, S., P. Y. Le Traon, and C. Le Provost, 2004: Mesoscale variability from a high-resolution model and from altimeter data in the North Atlantic Ocean. *J. Geophys. Res.,* **109,** C12025, doi:10.1029/2004JC002360.

Cuny, J. P., B. Rhines, P. P. Niiler, and S. Bacon, 2002: Labrador Sea boundary currents and the fate of the Irminger Sea Water. *J. Phys. Oceanogr.,* **32,** 627–647.

Fanning, A. F., and A. J. Weaver, 1997: A horizontal resolution and parameter sensitivity study of heat transport in an idealized coupled climate model. *J. Climate,* **10,** 2469–2478.

Fox-Kemper, B., R. Ferrari, and R. Hallberg, 2008: Parameterization of mixed layer eddies. Part I: Theory and diagnosis. *J. Phys. Oceanogr.,* **38,** 1145–1165.

Gawarkiewicz, G. G., and D. C. Chapman, 1995: A numerical study of dense water formation and transport on a shallow, sloping continental shelf. *J. Geophys. Res.,* **100,** 4489–4507.

Haine, T. W. N., and J. Marshall, 1998: Gravitational, symmetric, and baroclinic instability of the ocean mixed layer. *J. Phys. Oceanogr.,* **28,** 634–658.

Hoskins, B. J., 1975: The geostrophic momentum approximation and the semi-geostrophic equations. *J. Atmos. Sci.,* **32,** 233–242.

Jiang, L., and R. W. Garwood, 1996: Three-dimensional simulations of overflows on continental slopes. *J. Phys. Oceanogr.,* **26,** 1214–1233.

Marotzke, J., and J. R. Scott, 1999: Convective mixing and the thermohaline circulation. *J. Phys. Oceanogr.,* **29,** 2962–2970.

Marshall, J., and F. Schott, 1999: Open-ocean convection: Observations, theory, and models. *Rev. Geophys.,* **37,** 1–64.

——, C. Hill, L. Perelman, and A. Adcroft, 1997: Hydrostatic, quasi-hydrostatic, and nonhydrostatic ocean modeling. *J. Geophys. Res.,* **102,** 5733–5752.

Mauritzen, C., 1996a: Production of dense overflow waters feeding the North Atlantic across the Greenland–Scotland Ridge. Part 1: Evidence for a revised circulation scheme. *Deep-Sea Res.,* **43,** 769–806.

——, 1996b: Production of dense overflow waters feeding the North Atlantic across the Greenland–Scotland Ridge. Part 2: An inverse model. *Deep-Sea Res.,* **43,** 807–835.

Orlanski, I., 1976: A simple boundary condition for unbounded hyperbolic flows. *J. Comput. Phys.,* **21,** 251–269.

Pedlosky, J., 2003: Thermally driven circulations in small ocean basins. *J. Phys. Oceanogr.,* **33,** 2333–2340.

——, 2009: The response of a weakly stratified layer to buoyancy forcing. *J. Phys. Oceanogr.,* in press.

Phillips, N. A., 1954: Energy transformations and meridional circulations associated with simple baroclinic waves in a two-level, quasigeostrophic model. *Tellus,* **6,** 273–286.

Pickart, R. S., and M. A. Spall, 2007: Impact of Labrador Sea convection on the North Atlantic meridional overturning circulation. *J. Phys. Oceanogr.,* **37,** 2207–2227.

Polzin, K. L., J. M. Toole, J. R. Ledwell, and R. W. Schmitt, 1997: Spatial variability of turbulent mixing in the abyssal ocean. *Science,* **276,** 93–96.

Price, J. F., and M. O. Baringer, 1994: Outflows and deep water production by marginal seas. *Prog. Oceanogr.,* **33,** 161–200.

Schott, F., M. Visbeck, and J. Fischer, 1993: Observations of vertical currents and convection in the central Greenland Sea

during the winter of 1988–1989. *J. Geophys. Res.,* **98,** 14 401–14 421.

Send, U., and J. C. Marshall, 1995: Integral effects of deep convection. *J. Phys. Oceanogr.,* **25,** 855–872.

Spall, M. A., 2003: On the thermohaline circulation in flat bottom marginal seas. *J. Mar. Res.,* **61,** 1–25.

——, 2004: Boundary currents and water mass transformation in marginal seas. *J. Phys. Oceanogr.,* **34,** 1197–1213.

——, and R. S. Pickart, 2001: Where does dense water sink? A subpolar gyre example. *J. Phys. Oceanogr.,* **31,** 810–826.

Steffen, E. L., and E. A. D'Asaro, 2002: Deep convection in the Labrador Sea observed by Lagrangian floats. *J. Phys. Oceanogr.,* **32,** 475–492.

Stewartson, K., 1957: On almost rigid motions. *J. Fluid Mech.,* **3,** 17–26.

Stone, P. H., 1966: On non-geostrophic baroclinic instability. *J. Atmos. Sci.,* **23,** 390–400.

Thomas, L. N., 2005: Destruction of potential vorticity by winds. *J. Phys. Oceanogr.,* **35,** 2457–2466.

——, A. Tandon, and A. Mahadevan, 2008: Submesoscale processes and dynamics. *Eddy-Resolving Ocean Modeling, Geophys. Monogr*., Vol. 177, Amer. Geophys. Union, 17–38.

Walin, G., G. Broström, J. Nilsson, and O. Dahl, 2004: Baroclinic boundary currents with downstream decreasing buoyancy: A study of an idealized Nordic Seas system. *J. Mar. Res.,* **62,** 517–543.

Yoshikawa, Y., K. Akitomo, and T. Awajo, 2001: Formation process of intermediate water in a baroclinic current under cooling. *J. Geophys. Res.,* **106,** 1033–1051.